Generation and Evolution of High-Mach-Number Laser-Driven Magnetized Collisionless Shocks in the Laboratory

D. B. Schaeffer,[1,*] W. Fox,[2] D. Haberberger,[3] G. Fiksel,[4] A. Bhattacharjee,[1,2]
D. H. Barnak,[3,5] S. X. Hu,[3] and K. Germaschewski[6]
[1]Department of Astrophysical Sciences, Princeton University, Princeton, New Jersey 08540, USA
[2]Princeton Plasma Physics Laboratory, Princeton, New Jersey 08543, USA
[3]Laboratory for Laser Energetics, University of Rochester, Rochester, New York 14623, USA
[4]Center for Ultrafast Optical Science, University of Michigan, Ann Arbor, Michigan 48109, USA
[5]Fusion Science Center for Extreme States of Matter, University of Rochester, Rochester, New York 14623, USA
[6]Space Science Center, University of New Hampshire, Durham, New Hampshire 03824, USA
(Received 14 March 2017; published 13 July 2017)

We present the first laboratory generation of high-Mach-number magnetized collisionless shocks created through the interaction of an expanding laser-driven plasma with a magnetized ambient plasma. Time-resolved, two-dimensional imaging of plasma density and magnetic fields shows the formation and evolution of a supercritical shock propagating at magnetosonic Mach number $M_{ms} \approx 12$. Particle-in-cell simulations constrained by experimental data further detail the shock formation and separate dynamics of the multi-ion-species ambient plasma. The results show that the shocks form on time scales as fast as one gyroperiod, aided by the efficient coupling of energy, and the generation of a magnetic barrier between the piston and ambient ions. The development of this experimental platform complements present remote sensing and spacecraft observations, and opens the way for controlled laboratory investigations of high-Mach number collisionless shocks, including the mechanisms and efficiency of particle acceleration.

DOI: 10.1103/PhysRevLett.119.025001

Shocks act to convert incoming supersonic flows to heat, and in collisionless plasmas the shock layer forms on kinetic plasma scales through collective electromagnetic effects. These collisionless shocks have been observed in many space and astrophysical systems, including around Earth and planets of the solar system [1,2], the heliopause [3], and supernovae remnants [4]. Additionally, collisionless shocks are believed to accelerate particles, including cosmic rays, to extremely high energies [5,6]. Of particular importance are the class of supercritical [7] ($M_A \gtrsim 3$) and high-Mach-number shocks, which must reflect significant numbers of particles back into the upstream to accommodate entropy production, and in doing so seed proposed particle acceleration mechanisms [8,9].

In many of these systems, the shocks are *magnetized* due to preexisting magnetic fields in the upstream plasma. In the heliosphere magnetized shocks have been well studied within the limitations implied by 1D spacecraft trajectories. However, with the exception of some remotely sensed shocks driven by coronal mass ejections [10], it has, in general, not been possible to directly probe (via *in situ* means) the formation process(es) for heliospheric shocks. Meanwhile, remote sensing has provided compelling evidence that supernovae remnant shocks are driven by magnetically coupled pistons [4], but such observations are too distant and too late in time to resolve details of the initial piston-shock interaction. As a result, studies of collisionless shock formation have been mostly limited to numerical simulations [11] and lack empirical verification. Laboratory experiments—with their reproducibility and comprehensive, multidimensional data sets—can thus complement spacecraft and remote sensing observations through an appropriate scaling of key dimensionless parameters [12].

Here we present the first laboratory observation of the formation of high-Mach-number magnetized collisionless shocks created through the interaction of an expanding laser-driven plasma with a magnetized ambient plasma. We measure numerous features of collisionless shocks, including formation time scales, shock speed, magnetic and density compression ratios, and widths of the density jumps. These experiments were carried out on the Omega EP laser facility [13] at the University of Rochester. Plastic (CH) piston targets were embedded in an externally applied magnetic field and irradiated by high-energy lasers, driving supersonic plasma plumes through a preformed, magnetized ambient CH plasma in a perpendicular magnetic geometry. This experimental configuration utilizes the concept of a magnetically coupled piston pioneered by early experiments [14,15], and has been previously used to demonstrate how expanding, laser-driven piston plumes sweep up and compress the ambient plasma and magnetic field [16]. It also extends previous, low-Mach-number shock experiments [17–19] to a significantly new parameter space, with magnetic fields, ambient densities, and laser energies that are orders of magnitude larger, allowing higher Mach numbers over smaller spatial scales. Other versions of this configuration have focused on the formation of nonmagnetized (electrostatic) collisionless shocks [20–23]

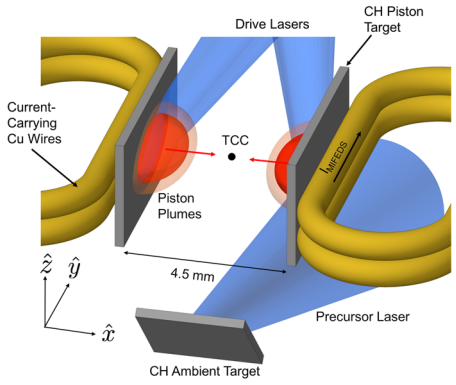

FIG. 1. Experimental setup. An external magnetic field was applied by pulsing current through conductors located behind opposing plastic (CH) piston targets. The volume between the piston targets was prefilled with an ambient plasma irradiated by a low-energy beam from a third CH target. Two counterpropagating piston plasma plumes, generated by ablating the opposing piston targets with two high-energy beams, were then driven through the magnetized ambient plasma. The resulting interaction was diagnosed with 2D refractive imaging (line-integrated along $\hat{z}$) and proton radiography (line-integrated along $\hat{y}$).

or counterstreaming geometries relevant to Weibel-mediated shocks [24,25].

The experimental setup is shown in Fig. 1. Two opposing plastic (CH) piston targets, separated by 4.5 mm, were each irradiated by a 5×10^{13} W/cm^2 drive beam (351 nm, 1.5 kJ, 2 ns) at time t_0, generating counterpropagating supersonic plasma plumes. The drive beams passed through a beam-smoothing phase plate and were incident on the piston targets at an angle of 74°, yielding an elliptical focal spot with a minor diameter of 0.9 mm and a major diameter of 3.1 mm. The piston targets were embedded in an externally imposed background magnetic field, oriented perpendicularly to the piston plasma flow and timed so that the drive beams fired at peak magnetic field ($B_{0z,\,\mathrm{peak}} = 8 \pm 1$ T). A third ambient CH target was placed 5 mm from the center point between the piston targets and was irradiated by a 9×10^{12} W/cm^2 precursor beam (351 nm, 100 J, 1 ns) to create a low-density ambient plasma. To allow time for the ambient plasma to prefill the volume between the piston targets, the precursor beam was timed 12 ns before t_0. There is no significant distortion of the external magnetic field due to this ambient expansion, as evidenced by proton radiographic images that show that the area between the targets remains uniform until the piston plasmas arrive. This also implies that the magnetic field diffuses anomalously fast into the magnetic cavity created by the ambient plasma, as observed elsewhere [18,26].

The interaction of the piston plasmas with the magnetized ambient plasma was diagnosed with a 263 nm probe beam (10 ps) that passed through the plasmas, producing simultaneous images of shadowgraphy and angular filter refractometry (AFR) [27]. AFR maps the angles by which the probe beam is refracted to a finite set of imaged bands whose spatially resolved edges correspond to known values of the line-integrated first derivative of density. Shadowgraphy similarly measures the line-integrated second derivative of density, but does so continuously across the image. Additionally, the dynamics and topology of the magnetic fields were probed using a multi-MeV proton beam generated with an independent short-pulse laser in the same configuration as discussed in Ref. [24]. The deflection of the protons as they pass through the interacting plasmas are then collected on several energy-resolved image plates, which can be used to estimate the topology and magnitude of the magnetic field [28].

Figure 2 shows AFR and proton radiographic images. The main features seen in the AFR images include two wide bands (additional bands can also be seen near the targets), and, in some conditions, one or two very narrow bands near the image center. These narrow bands are also seen in the same locations in the corresponding shadowgraphy images. The wide bands are associated with the piston plasma plumes, while the narrow bands indicate the development of very strong density gradients where the piston and ambient plasmas interact. Figures 2(b)–2(d), for which $B_0 > 0$ and $n_0 > 0$, show the formation and evolution of shocklike features from early to late times. We note that shock formation only requires a single piston plume interacting with the ambient plasma [see Fig. 2(b)]; multiple pistons were used to increase data collection. Figure 2(e) is a proton radiographic image and shows the formation of strong magnetic field compressions (light regions of low proton fluence) coincident with the AFR shock bands, as well as the formation of magnetic cavities (dark regions) behind the magnetic compressions. Two null tests were also carried out. Figure 2(a) shows that without an external magnetic field ($B_0 = 0$) and without an ambient plasma ($n_0 = 0$), only the piston plumes are visible. Unexpectedly, with an ambient plasma but without an external field we still observed leading bands; however, these bands were 3 times wider than those observed with an external field. We are able to obtain such broadening in simulations with weak magnetic fields ($B_0 < 1$ T). One possible source may be Biermann-battery-generated magnetic fields advected with the laser plasmas, which have of order 1%–10% of the magnetic energy of the externally imposed magnetic field.

The experiments were simulated with the 2D particle-in-cell (PIC) PSC [29] and 2D radiation-hydrodynamic DRACO [30] codes. DRACO was used to model the laser-target interaction in order to predict the density and temperature profiles of the ambient and piston plasmas; the associated wide plume bands imaged through AFR were found to be in good agreement with these DRACO predictions. Modeling by DRACO further indicated that the ambient plasma electron density and temperature remain relatively stable at $n_{e0} \approx 0.6 \times 10^{19}$ cm^{-3} and $T_{e0} \approx 15$ eV between the piston targets over the time scales of the experiment. We used these plume parameters to initialize a fully kinetic PSC simulation of the expansion of a mixed-species CH piston plasma into a uniform, preformed ambient CH plasma embedded in a

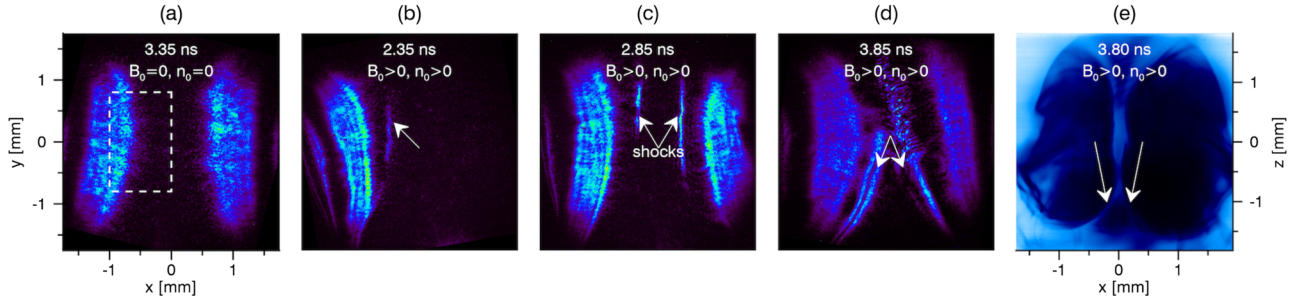

FIG. 2. Refractive and proton radiographic images of collisionless shock evolution. In each image, the piston targets are located just outside the left and right borders, while the ambient target is located below the bottom border. The piston plasmas expand toward the center ($x = 0$). The time stamps correspond to the time relative to the firing of the drive beams. The dashed rectangle in (a) represents the region of interest in Fig. 3. Panels (a)–(d) are images of angular filter refractometry. In (a), no shock is observed without an external magnetic field or ambient plasma. In (b)–(d), the shock is observed evolving from early to late times with an external field and ambient plasma. In (b), only one target was used, confirming that these features are independent of counterstreaming interactions between two pistons. In (e), proton radiography reveals the formation of strong magnetic field compressions (light ribbons) coincident with the shock at comparable times.

uniform magnetic field. Like the DRACO runs, the PIC simulations were validated against experimental data by comparing observed AFR features with those synthetically generated through PSC. In particular, we conducted a sensitivity scan of the effect of upstream density on shock formation, varying the ambient density by an order of magnitude around the DRACO-predicted value. We find robust collisionless shock formation over a wide range of densities but obtain best agreement between observed and simulated features at $n_{e0} = (0.6 \pm 0.3) \times 10^{19}$ cm^{-3}, which we therefore use for all relevant calculations. We note that fluctuations around this density were too small to be directly measured by the AFR diagnostic.

Density profiles reconstructed from the refractive images are shown in Fig. 3. These profiles and associated numerical modeling show conclusive evidence of the production of a supercritical magnetized collisionless shock, as indicated by a magnetosonic Mach number $M_{\rm ms} > 4$, a magnetic compression $B/B_0 > 2$, a density compression $n/n_0 > 2$, a compression ramp width $\Delta x/d_i > 1$ ($d_i = c/\omega_{pi}$), and the separation of the shock structure from the piston. The speed of the narrow bands in Fig. 2 can be estimated from their time of flight. Between 2.35 and 2.85 ns, it is found to be $v_s = 700 \pm 30$ km/s. This implies that the AFR bands are moving highly supermagnetosonically with $M_{\rm ms} = v_s/c_{\rm ms} = 12 \pm 4$, where $c_{\rm ms}^2 = v_A^2 + c_s^2$, v_A is the Alfvén speed, and c_s is the sound speed. Here, the speeds are calculated relative to the upstream ambient C plasma and peak magnetic field. At these speeds, the ions are effectively collisionless, with a collisional length scale larger than the distance between the piston targets.

Figures 3(a)–3(b) show that as the AFR bands propagate, their corresponding jump in density grows from $\Delta n_e = (1.3 \pm 0.3) \times 10^{19}$ cm^{-3} at 2.35 ns to $\Delta n_e = (1.6 \pm 0.3) \times 10^{19}$ cm^{-3} at 2.85 ns. These density jumps represent a growth in the maximum compression ratio relative to the background of $n_e/n_{e0} = 3.2 \pm 0.5$ to $n_e/n_{e0} = 3.7 \pm 0.5$. Simultaneously, the width of the density jump grows from $\Delta x/d_{i0} = 0.6 \pm 0.2$ to $\Delta x/d_{i0} = 1.0 \pm 0.2$, where d_{i0} is the upstream ambient C ion inertial length and is the natural lower bound condition for the shock thickness. Note that the measured widths are still consistent with shock widths that are typically on the order of the downstream ambient ion gyroradius ρ_i [31]. This is because $\rho_i \sim 3d_{i0}$, and the

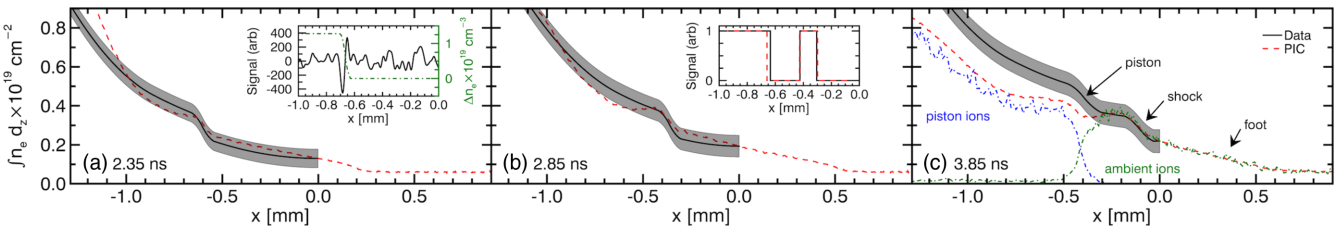

FIG. 3. Evolution of line-integrated electron density profiles at (a) 2.35, (b) 2.85, and (c) 3.85 ns after laser ablation. For each, the density profiles (black) were reconstructed by linearly interpolating between the gradient density values associated with each AFR band edge and, in the regions of the density jumps, utilizing the shadowgraphy profiles. The constant density offset was estimated from simulations, and the shaded band corresponds to the uncertainty in this offset. Also shown are the corresponding profiles from PSC PIC simulations (red). Additionally, in (c) the ambient (green) and piston (blue) contributions to the total electron density in the PIC simulations are shown. [(a), inset] Raw shadowgraphy signal (black) and reconstructed relative density (green) profile at 2.35 ns. [(b), inset] Direct comparison of the raw AFR signal (black) and corresponding synthetic simulation signal (red) at 2.85 ns. For both, the signals have been reduced to binary for simplicity. In all plots, the plasma moves toward $x = 0$.

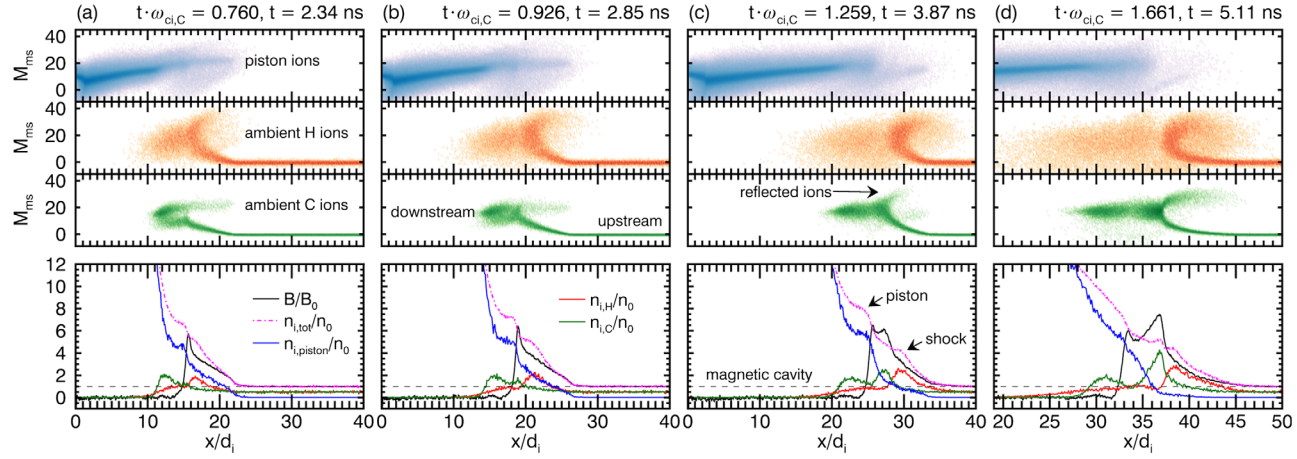

FIG. 4. Results from 2D particle-in-cell simulations that show the formation of a high-Mach-number magnetized collisionless shock. The simulations consist of a CH piston plasma expanding into a CH ambient plasma in an externally applied magnetic field. Each panel is representative of a different time in units of the upstream C ion gyroperiod $\omega_{ci,C}^{-1}$, from earliest (a) to latest (d). For each panel, the top three rows are phase space density plots of piston, ambient H, and ambient C ions in terms of the C magnetosonic Mach number M_{ms} and ambient C ion inertial length d_i. The bottom row are plots of magnetic field (black), total ion density (purple), ambient H ion density (red), ambient C ion density (green), and piston ion density (blue) relative to their upstream ambient values.

refractive diagnostics are only sensitive to the subsection of the shock ramps with the largest density gradients. Indeed, PIC simulations indicate that the width of the shock ramps is on the order of ρ_i.

Figure 2(d) shows that by 3.85 ns, the leading AFR band has bifurcated into two bands, which leads to a double "bump" feature in the extrapolated density profile in Fig. 3(c). The frontmost band is similar to the leading band at 2.85 ns, while the second band is wider with $\Delta x/d_{i0} = 1.3 \pm 0.2$ and a density jump of $\Delta n_e = (1.5 \pm 0.3) \times 10^{19}$ cm^{-3}. However, only the frontmost AFR band has a corresponding shadowgraphy signal, indicating that the two AFR bands represent two distinct features, rather than a single large density gradient that encompasses two bands. We can also estimate the magnetic field compression by comparing the proton fluence in the "ribbon" region to the fluence in the magnetic cavity in Fig. 2(e). Following Ref. [28], the magnetic field in the object plane is given by $\nabla_\perp \int \tilde{\mathbf{B}} \times d\ell \approx \tilde{B}_z L_y/L_x \sim 140$ T, where L_y is the path integration length and L_x is a characteristic gradient length scale on the order of d_{i0}. Note that $\tilde{B}_z$ is *in addition* to the background magnetic field, so that $B_z = \tilde{B}_z + B_{0z}$, where the average background field $B_{0z} \sim 4$ T. We find at 3.80 ns and in the region coincident with the narrow AFR bands, the magnetic field is compressed by $B_z/B_{0z} \approx 3$ and is fully expelled ($B_z \approx 0$) behind the compression.

Figure 4 shows that these experimental features are reproduced by PIC simulations. By 2.35 ns [$t \sim 1.4\ \omega_{ci,H}^{-1} = 0.7\ \omega_{ci,C}^{-1}$, Fig. 4(a)], a collisionless shock has already formed in the ambient H ions and is moving at $M_{ms} \sim 15$. This can be seen by the large density and magnetic field compressions ($n/n_0 > 3$, $B/B_0 > 3$), the large compression ramp widths ($\Delta x/\rho_i \sim 1$), a population of hot downstream H ions (in the shock frame, they are heated as they are decelerated through the shock front), and a small population of highly accelerated ambient H ions (in the shock frame, these are reflected ions). By 2.85 ns [$t \sim 0.9\ \omega_{ci,C}^{-1}$, Fig. 4(b)], a C shock has also formed slightly downstream of the H shock. Figure 4(c) shows that by 3.85 ns ($t \sim 1.3\omega_{ci,C}^{-1}$) a double bump feature appears in the total density profile. The two bumps correspond to individual compressions of ambient and piston ions, and indicate that the H and C shocks are separating from the piston. At later times [Fig. 4(d)], the combined C and H shocks further decouple from the piston, and a downstream component in the density and magnetic field profiles begins to form.

These results are the first to experimentally show collisionless shock formation on time scales as fast as one gyroperiod ω_{ci}^{-1}. The experimentally constrained PIC simulations indicate that these fast formation time scales are possible due to two effects. The first is the efficient coupling of piston energy to the ambient ions. This is accomplished through the generation of strong $\mathbf{J_p} \times \mathbf{B}$ electric fields (i.e., Larmor coupling [32,33]), which are created as the piston ion "current" moves across the background magnetic field, and which accelerate ambient ions to of order the piston speed within ω_{ci}^{-1}. Simultaneously, the piston expansion drives a diamagnetic current that creates a leading magnetic compression and trailing magnetic cavity [34]. The second effect is the trapping of piston ions behind the magnetic compression. This effect becomes more pronounced with time and allows accelerated ambient ions to interact unimpeded with upstream ambient ions. Within one ω_{ci}^{-1}, the intensification of the magnetic compression due to the pile up of accelerated ambient ions results in a significant expulsion of piston ions from the leading edge of the expansion. These effects are manifested in the size and timing of the experimental features. The pileup of trapped

piston ions results in density gradients over length scales of order the compressed gyroradius ρ_i (a few d_{i0}), which show up as narrow AFR bands. As more piston ions become trapped and the ambient ion density becomes dominant ahead of the magnetic compression, two density gradients associated with each population appear, resulting in the two observed narrow AFR bands.

In this Letter we have demonstrated that high-Mach-number magnetized collisionless shocks can be generated in the laboratory, which opens a new experimental regime for studying shock formation and evolution that is difficult to achieve with spacecraft. The experimental platform is highly flexible, allowing variation in the applied magnetic field, upstream density, magnetic geometry, and piston speed. Its development enables new studies on the relationship between collisionless shocks and particle acceleration, and with extensions to the larger system sizes available on platforms such as the National Ignition Facility, new collaborative investigations between shocks and other strongly driven, astrophysically relevant systems such as those involving magnetic reconnection or the Weibel instability.

We thank the staff of the Omega EP facility for their help in executing these experiments. Time on the Omega EP facility was funded by the Department of Energy (DOE) through Grant No. DE-NA0002731. The PIC simulations were conducted on the Titan supercomputer at the Oak Ridge Leadership Computing Facility at the Oak Ridge National Laboratory, supported by the Office of Science of the DOE under Contract No. DE-AC05-00OR22725. This research was also supported by the DOE under Contracts No. DE-SC0008655 and No. DE-SC0016249.

*dereks@princeton.edu

[1] E. J. Smith, L. Davis, D. E. Jones, P. J. Coleman, D. S. Colburn, P. Dyal, and C. P. Sonett, Jupiter's magnetic field. magnetosphere, and interaction with the solar wind: Pioneer 11, Science **188**, 451 (1975); E. J. Smith, L. Davis, D. E. Jones, P. J. Coleman, D. S. Colburn, P. Dyal, and C. P. Sonett, Saturn's magnetic field and magnetosphere, Science **207**, 407 (1980).

[2] A. H. Sulaiman, A. Masters, M. K. Dougherty, D. Burgess, M. Fujimoto, and G. B. Hospodarsky, Quasiperpendicular high Mach number shocks, Phys. Rev. Lett. **115**, 125001 (2015).

[3] L. F. Burlaga, N. F. Ness, M. H. Acuña, R. P. Lepping, J. E. P. Connerney, and J. D. Richardson, Magnetic fields at the solar wind termination shock, Nature **454**, 75 (2008).

[4] D. S. Spicer, S. P. Maran, and R. W. Clark, A model of the pre-Sedov expansion phase of supernova remnant-ambient plasma coupling and x-ray emission from SN 1987a, Astrophys. J. **356**, 549 (1990).

[5] A. Masters *et al.*, Electron acceleration to relativistic energies at a strong quasi-parallel shock wave, Nat. Phys. **9**, 164 (2013).

[6] M. Ackermann *et al.*, Detection of the characteristic pion-decay signature in supernova remnants, Science **339**, 807 (2013).

[7] A. Balogh and R. A. Treumann, *Physics of Collisionless Shocks*, *series Scientific Report Series* (Springer, New York, 2013), Vol. 12.

[8] D. Caprioli and A. Spitkovsky, Simulations of ion acceleration at non-relativistic shocks. i. acceleration efficiency, Astrophys. J. **783**, 91 (2014).

[9] Y. Matsumoto, T. Amano, T. N. Kato, and M. Hoshino,, Stochastic electron acceleration during spontaneous turbulent reconnection in a strong shock wave, Science **347**, 974 (2015).

[10] S. T. Lepri, J. M. Laming, C. E. Rakowski, and R. von Steiger, Spatially dependent heating and ionization in an icme observed by both ace and ulysses, Astrophys. J. **760**, 105 (2012).

[11] D. Winske and S. P. Gary, Hybrid simulations of debris-ambient ion interactions in astrophysical explosions, J. Geophys. Res. **112**, A10303 (2007).

[12] R. P. Drake, The design of laboratory experiments to produce collisionless shocks of cosmic relevance, Phys. Plasmas **7**, 4690 (2000).

[13] L. Waxer *et al.*, High-energy petawatt capability for the Omega laser, Opt. Photonics News **16**, 30 (2005).

[14] J. W. M. Paul, L. S. Holmes, M. J. Parkinson, and J. Sheffield, Experimental observations on the structure of collisionless shock waves in a magnetized plasma, Nature **208**, 133 (1965).

[15] A. Y. Cheung, R. R. Goforth, and D. W. Koopman, Magnetically induced collisionless coupling between counterstreaming laser-produced plasmas, Phys. Rev. Lett. **31**, 429 (1973).

[16] G. Fiksel, W. Fox, A. Bhattacharjee, D. H. Barnak, P.-Y. Chang, K. Germaschewski, S. X. Hu, and P. M. Nilson, Magnetic reconnection between colliding magnetized laser-produced plasma plumes, Phys. Rev. Lett. **113**, 105003 (2014).

[17] C. Niemann *et al.*, Observation of collisionless shocks in a large current-free laboratory plasma, Geophys. Res. Lett. **41**, 7413 (2014).

[18] D. B. Schaeffer, E. T. Everson, D. Winske, C. G. Constantin, A. S. Bondarenko, L. A. Morton, K. A. Flippo, D. S. Montgomery, S. A. Gaillard, and C. Niemann, Generation of magnetized collisionless shocks by a novel, laser-driven magnetic piston, Phys. Plasmas **19**, 070702 (2012).

[19] D. B. Schaeffer, E. T. Everson, A. S. Bondarenko, S. E. Clark, C. G. Constantin, D. Winske, W. Gekelman, and C. Niemann, Experimental study of subcritical laboratory magnetized collisionless shocks using a laser-driven magnetic piston, Phys. Plasmas **22**, 113101 (2015).

[20] L. Romagnani *et al.*, Observation of collisionless shocks in laser-plasma experiments, Phys. Rev. Lett. **101**, 025004 (2008).

[21] Y. Kuramitsu *et al.*, Time evolution of collisionless shock in counterstreaming laser-produced plasmas, Phys. Rev. Lett. **106**, 175002 (2011).

[22] H. Ahmed *et al.*, Time-resolved characterization of the formation of a collisionless shock, Phys. Rev. Lett. **110**, 205001 (2013).

[23] D. Haberberger *et al.*, Collisionless shocks in laser-produced plasma generate monoenergetic high-energy proton beams, Nat. Phys. **8**, 95 (2011).

[24] W. Fox, G. Fiksel, A. Bhattacharjee, P.-Y. Chang, K. Germaschewski, S. X. Hu, and P. M. Nilson, Filamentation instability of counterstreaming laser-driven plasmas, Phys. Rev. Lett. **111**, 225002 (2013).

[25] C. M. Huntington *et al.*, Observation of magnetic field generation via the Weibel instability in interpenetrating plasma flows, Nat. Phys. **11**, 173 (2015).

[26] N. Brenning, R. L. Merlino, D. Lundin, M. A. Raadu, and U. Helmersson, Faster-than-Bohm Cross-B electron transport in strongly pulsed plasmas, Phys. Rev. Lett. **103**, 225003 (2009).

[27] D. Haberberger, S. Ivancic, S. X. Hu, R. Boni, M. Barczys, R. S. Craxton, and D. H. Froula, Measurements of electron density profiles using an angular filter refractometera, Phys. Plasmas **21**, 056304 (2014).

[28] N. L. Kugland, D. D. Ryutov, C. Plechaty, J. S. Ross, and H.-S. Park, Invited article: Relation between electric and magnetic field structures and their proton-beam images, Rev. Sci. Instrum. **83**, 101301 (2012).

[29] K. Germaschewski, W. Fox, S. Abbott, N. Ahmadi, K. Maynard, L. Wang, H. Ruhl, and A. Bhattacharjee, The plasma simulation code: A modern particle-in-cell code with patch-based load-balancing, J. Comput. Phys. **318**, 305 (2016).

[30] S. X. Hu *et al.*, Hydrodynamic simulations of long-scale-length two-plasmon–decay experiments at the omega laser facility, Phys. Plasmas **20**, 032704 (2013).

[31] S. D. Bale, F. S. Mozer, and T. S. Horbury, Density-transition scale at quasiperpendicular collisionless shocks, Phys. Rev. Lett. **91**, 265004 (2003).

[32] D. W. Hewett, S. H. Brecht, and D. J. Larson, The physics of ion decoupling in magnetized plasma expansions, J. Geophys. Res. **116**, A11310 (2011).

[33] A. S. Bondarenko *et al.*, Collisionless momentum transfer in space and astrophysical explosions, Nat. Phys. **13**, 573 (2017).

[34] T. P. Wright, Early-time model of laser plasma expansion, Phys. Fluids **14**, 1905 (1971).